ORIGINAL INNOVATION   **Open Access**

Numerical simulation and validation of local wind environment of twin-box girder with wind barriers

Fengying Wu[1], Lin Zhao[1*], Fengchan Cao[1] and Yaojun Ge[2]

*Correspondence:
zhaolin@tongji.edu.cn

[1] State Key Lab of Disaster Reduction in Civil Engineering, Tongji University, Shanghai 200092, China
[2] Key Laboratory of Transport Industry of Wind Resistant Technology for Bridge Structures, Tongji University, Shanghai 200092, China

Abstract

Computational fluid dynamics (CFD) was used to reproduce wind fields around a twin-box girder. Wind tunnel tests and field measurements were conducted to verify the accuracy of the CFD results. Variations in wind speed at different heights and crosswind reduction effects with different barriers were also examined using CFD simulation; the barriers had significant reduction effects. The reduction effectiveness was closely related to the barrier height and position; porosity was also a crucial factor. The wind speed profiles of a twin-box girder and a single box girder were analysed to determine why the wind speeds above the downstream deck were lower than above the windward deck of the twin-box girder. The results show that the incoming flow leaked downward through the slotted parts of the bridge and formed regulation vortices. Wind speeds were lower above the downstream deck than above the upstream deck as a result of leakage effects. The gap width also influenced the wind environment around the bridge deck.

Keywords: Wind barriers, Twin-box girder, Local wind environment, Crosswind reduction factor, CFD, Wind tunnel test, Field measurement

1 Introduction

With increasing construction of long-span bridges and more complicated wind environments around bridge decks, wind loads have become the primary control factor for long-span bridges. High wind speeds produce bridge safety issues (Zhang et al., 2018), threaten vehicle driving safety, and reduce driving comfort (Lin et al., 2018). Strong crosswinds on the Humen suspension bridge in China on 11 August 2004 caused tall vehicles to overturn while driving (Fig. 1a); similar accidents occurred on the Minjiang cable-stayed bridge in China in 2005 (Fig. 1b) (Zhu et al., 2012), resulting in severe economic losses and negative publicity (Gawthorpe, 1994). Further study is necessary to reduce risks to vehicles in strong winds and improve long-span bridge serviceability in severe weather conditions. To improve driving safety on long-span bridges, in addition to vehicle shape optimisation to reduce wind loads (Buljac et al., 2020), appropriate wind barriers can decrease crosswind speeds and aerodynamic effects on vehicles and improve driving comfort on long-span bridges (Zou et al., 2016). Wind barriers have

(a) vehicle accident on Humen bridge   (b) vehicle accident on Minjiang bridge

Fig. 1 Vehicles overturned by crosswind

Table 1 Review of crosswind reduction effects of wind barriers

Researcher	Method	Topic
Judd et al., 1996	Wind tunnel test	overall shelter effectiveness of multiple array barrier greater than single barrier
Hong et al., 2015	CFD modelling	wind speed reduction of barrier fence prediction
Kozmar et al., 2012	Wind tunnel test	porosity and height as two key parameters, optimal barrier with 30% porosity and 5 m height
Frank and Ruck, 2005	Wind tunnel test	wind-protected area of consecutively arranged windbreaks larger than single windbreak
Dong et al., 2007	Wind tunnel test	optimal porosity approximately 0.2 or 0.3
Santiago et al., 2007	Numerical simulation	best porosity for downwind shelter is 0.35

been added to many long-span bridges to improve driving safety and comfort. Many studies have shown that crosswind speed can be significantly reduced by wind barriers. Examples include the Severn suspension bridge, the Hangzhou Bay Bridge, and the Tsing Ma Bridge (Chu et al., 2013). Shielding effects and crosswind reduction effects of wind barriers are determined through wind tunnel testing and numerical simulation. Recent research developments are summarised in Table 1.

Wind barriers are critical for reducing wind and ensuring vehicle driving safety on long-span bridges in adverse weather conditions. However, current research continues to focus on numerical simulation and wind tunnel test methods to improve wind barrier application; full-scale field measurement validation is still lacking. With the development of aerodynamics and fluid mechanics, and the rapid growth of computing capability, many discretion methods and calculation models for flow-field analysis based on CFD have been applied in engineering projects.

Wind barriers were adopted in bridge engineering to improve wind environment above the girder deck to ensure the vehicles driving safety and comfort under crosswind impact. But the reduction effect of wind barriers was depended on related factors, such as barrier types, porosity, height, location, etc. According to Hua, wind barrier can improve both flutter and VIV properties for bridges. However, Wu et al. (2023) found that vortex-induced vibrations may amplified by wind barriers. But Yang et al. (2023) also pointed out that the position of wind barriers is more important than shape. Chu
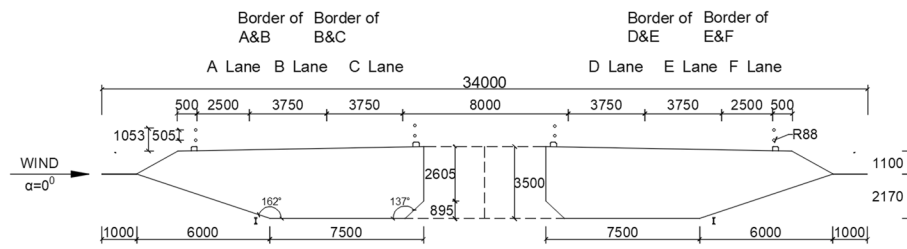
Fig. 2 Xihoumen bridge cross section (unit: mm)

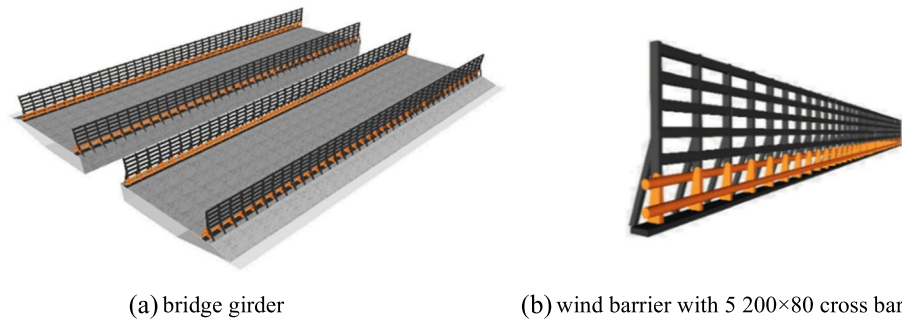(a) bridge girder   (b) wind barrier with 5 200×80 cross bars

Fig. 3 Schematic diagram of bridge and wind barriers

et al. (2013) investigated the effects of wind barrier on the side force on the moving vehicle, results shown that that the influence of wind barrier porosity is ignorable compared to the height of wind barrier. To ensure the safety of vehicles under high wind speed, 12 types of wind barrier with different porosity and different horizontal bar arrangements are analysed to gain a better reduction effect of crosswind. Appropriate selection of calculation models, discretion methods, and boundary conditions can provide better overall flow-field information, with small deviations between numerical results and actual conditions. The Xihoumen Bridge, with a main span of 1650 m, was considered as a case study to determine variations in the wind field around the bridge deck and height-related wind speeds, and the shielding effects of lateral incoming flow with and without wind barriers. The CFD results were verified through wind tunnel tests and field measurements, contributing to better application of CFD methods in wind barrier optimisation, and providing detailed descriptions of flow fields around girder deck.

2 Numerical simulation and validation

2.1 Simulation settings

The Xihoumen Bridge, a long-span suspension bridge with a main span of 1650 m, was studied for wind environment analysis in lateral flow considering different types of wind barriers. It is a twin-box bridge, with an overall width of 36.0 m, a height of 3.5 m, and a gap width of 6.0 m. The bridge section diagram and calculation lanes are shown in Fig. 2. The direction of the incoming flow was considered from lanes A to F above the bridge deck, and the wind attack angle was set as 0°. Figure 3 shows the bridge layout and local wind barriers. The wind barriers were set as five crossbars with cross-sections of 200 mm × 80 mm, as used in wind tunnel tests and practical applications for improving wind environments around bridge decks, especially at vehicle
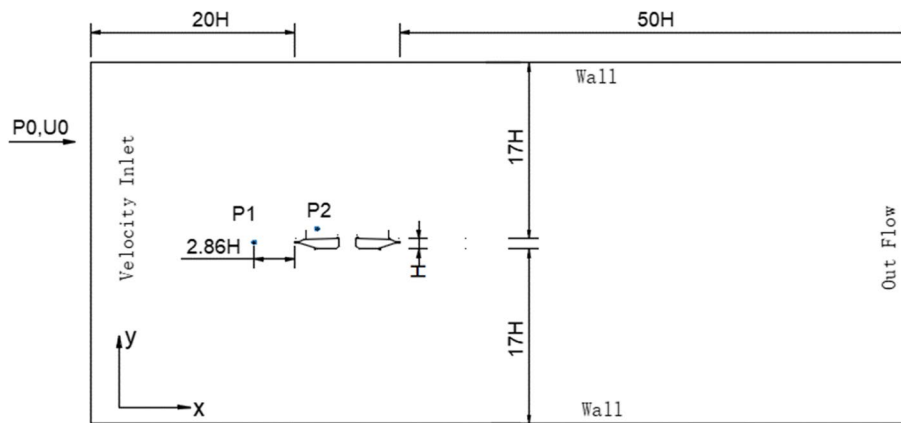
Fig. 4 Boundary conditions and computation domain setting

driving level. To ensure that the CFD results agreed with the measurement results, a full-scale model was used instead of a scale model for CFD simulation calculation.

2.2 Computation domain and boundary conditions

To avoid blockage interference, the computational domain was designed as a free-flow simulation environment. The rectangular simulation domain is shown in Fig. 4, with a height of 124 m and a width of 282 m, providing a blockage ratio of 0.023. The length of the incoming flow zone is 20 times greater than the height of the bridge girder; the length of the weak region is 50 times greater, and the upper and lower boundaries are 17 times greater. The boundary conditions and of the computation domain in the wind environment calculation are the same as for calculations without wind barriers.

The flow around the bridge deck was considered as an incompressible flow. The entrance condition of the computation domain was set as a velocity boundary condition, and the free outlet boundary was used as the outlet boundary condition. To improve the vehicle driving standard in typhoon and monsoon areas, the wind speed for driving safety was increased to 27 m/s. This value is slightly higher than the mean whole gale value of 26.5 m/s, which is the maximum navigable wind speed for ferryboats in Zhoushan areas. A uniform velocity profile was used. The velocity inlet boundary has typically been used (Hemida and Krajnovic, 2009; Morden et al., 2015) as it simplifies the method for defining characteristics. The non-slip solid wall boundary condition was considered as the boundary condition for the bridge section, the balustrade, and the wind barriers. The SIMPLE pressure–velocity coupled method was used to solve the pressure–velocity coupled field. The residual value was set to 10E-5 to meet the convergence criterion. The Reynolds number was sufficiently large to be considered as a constraint on the experimental conditions. The main objective of this study was to compare the crosswind reduction effects of different types of wind barriers. The Reynolds number had the same effect when the CFD method was used to analyse the reduction effects of wind barriers. Thus, it can be concluded that the Reynolds number has a limited influence on the case study results.

2.3 Mesh strategy and computational model

A turbulence flow can be divided into two parts as it flows over a boundary wall: the near-wall zone (inner zone) and the core zone (outer zone). The flow is fully developed in the outer zone but insufficiently developed in the inner zone. A transition occurs in the near-wall region, and laminar flow gradually develops into turbulence flow. To determine the governing flow in this area, two methods have been used: a multi-zone method and a method using approximate wall boundary conditions. For the multi-zone method, the size of the mesh element must be small to capture the tiny vortex structures in the near-wall region. A realisable $k–\varepsilon$ model based on the RANS simulation method is the most widely used model. It demonstrates excellent performance when used with related flows and is also used with different flow types for its simplicity and computation time savings (Tominaga and Stathopoulos, 2009). In addition, it has greater accuracy in predicting buoyancy effects, strong swirling flow, and high shear rates, indicating good performance and physical phenomenon prediction for most industrial flow issues.

The boundary layer flow near a wall is dominated by the viscous force, and there is insufficient room for development of turbulence. Thus, the flow-field calculation must be used with a special treatment method such as a wall function method because the realisable $k–\varepsilon$ model only works effectively with fully developed turbulence flow (Blocken et al., 2008). The wall functions apply the wall boundary conditions to all solution variables in the $k–\varepsilon$ turbulence model (Sarafrazi and Talaee, 2020). Different wall function methods have been implemented in the near-wall region and the outer zone using a semi-empirical formula (Ma et al., 2018). An incompressible flow with a high Reynolds number is solved using a high-Reynolds-number turbulence model and the wall function method. Y + is used to calculate the height of the first layer near the wall (Sarafrazi and Talaee, 2020):

$$y^+ = \frac{u^*y}{v} = \frac{y\sqrt{\tau_w/\rho}}{v} \qquad (1)$$

where u^* is the friction velocity; y is the distance from the wall; v is the dynamic viscosity; τ_w is the shear velocity of the wall, and ρ is the fluid density.

The realisable $k–\varepsilon$ model and the standard wall function method were used to simulate the 2-D flow around the bridge deck section.

A triangular mesh element was used in the numerical simulation analysis; an unstructured mesh was used for computation domain discretion to consider the complexity of the bridge geometry, and for efficient simulation resolution. All numerical simulations were conducted using the same Reynolds number ($Re = U_\infty D/v = 6.39 \times 10^6$), corresponding to a wind speed of 27 m/s. To capture the flow characteristics of these regions, a very fine mesh must be used.

High-quality mesh is necessary to ensure calculation stability and accuracy, and reduce nonphysical solutions in the calculation process (Wilson, 1985). To this end, a refined mesh must be applied to capture the flow characteristics of these regions. Therefore, high-quality mesh elements not only ensure the stability and correctness of the calculation results but also effectively reduce the nonphysical solutions of the calculation process (Wilson, 1985).
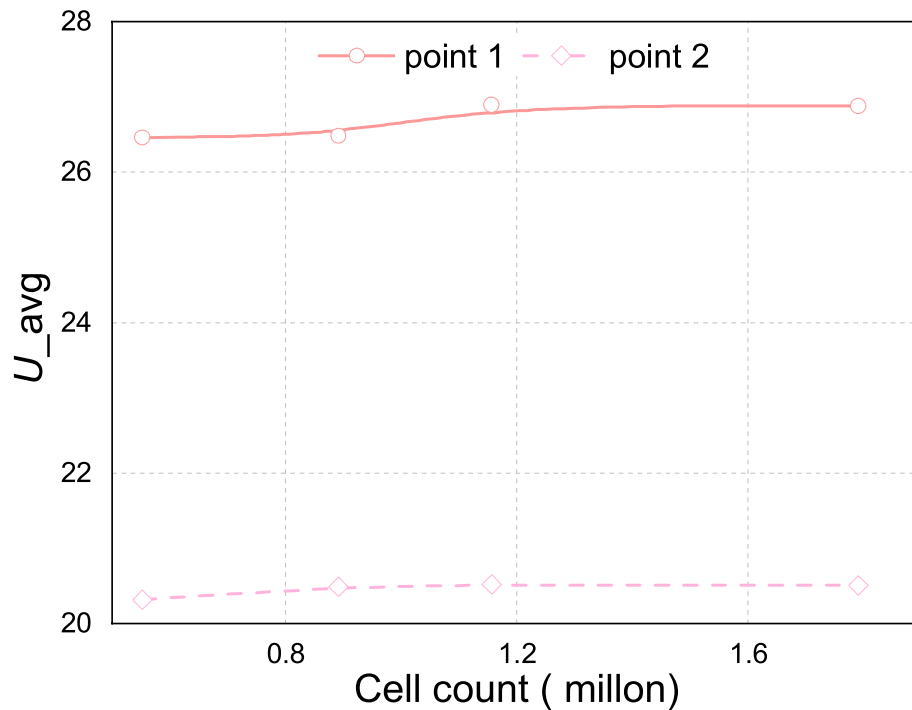
Fig. 5 Mesh density independence

Table 2 Properties of mesh refinement

Mesh	Cell count (millions)	Cd	Estimated uncertainty/error
Coarse	0.553	0.646	±0.06
Medium	0.892	0.988	±0.01
Fine	1.157	1.041	±0.04
Wind tunnel test	-	1.07	

A mesh density sensitivity study was conducted to evaluate the mesh; the refinements did not generate considerable deviation in the numerical simulation. To develop a superior mesh strategy, a mesh density independence study was conducted. Wind speeds with the four mesh types at monitor points 1 and 2 (Fig. 4) were compared with different densities as the calculation converged, as shown in Fig. 5. The results vary as the mesh density increases. However, with 1.157E6 total mesh elements, the results tended to stabilise as the number of grids increased. There was no evident disparity when the grid number increased to 1.791E6; mesh independence was achieved. The properties of different meshes are summarised in Table 2. The drag coefficient obtained from the wind tunnel test was used to verify the results of different mesh strategies. The results with fine mesh were closer to the wind tunnel test results, verifying the calculation accuracy. Considering the force coefficients and the resulting computation time burden, the fine mesh scheme was used in subsequent comparison of wind speed reduction effects with different wind barrier schemes, using a total of 1.157E6 mesh elements. Figure 6 shows the planar mesh generation strategy. Chu et al. (2013) and Bendjebbas et al. (2018) also
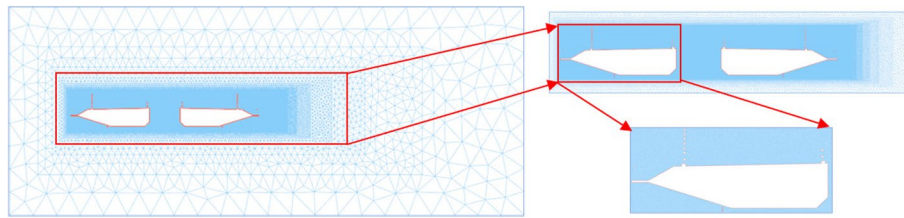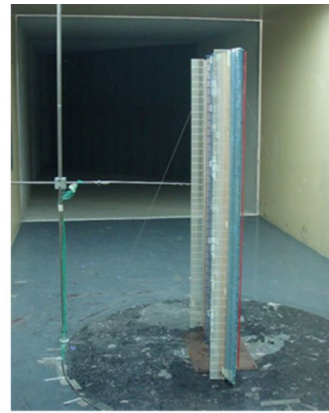
Fig. 6 Computation discretization

(a) girder without barriers   (b) girder with barriers (5 200×80 cross bar)

Fig. 7 Wind tunnel test and segmental model

analysed the influence of wind barriers on the surrounding wind field using unstructured mesh generation; the results showed that the mesh met the accuracy requirements and reduced the calculation time. A more precise mesh generation strategy for flow near a wall improves computational efficiency. In general, starting from the fine grid, the deviation between the solution and experimental results decreases, asymptoting to a grid-independent solution.

3 Validation and discussion

3.1 Wind tunnel test

To verify the accuracy of the numerical simulation results, a wind tunnel verification test was conducted in the TJ-2 wind tunnel at Tongji University to analyse the wind field around a bridge deck. The segmental model is shown in Fig. 7. The scale ratio of the model was 1:40, and the inflow wind speed was set to 10 m/s. Wind speed variation was analysed in different calculation lanes (boundary of A and B lanes, B lane, boundary of B and C lanes, D lane) at vertical heights of 2.0 m and 4.5 m above the bridge deck (vertical heights above the segmental model deck were 0.050 m and 0.113 m, respectively) with and without wind barriers (five 200 mm × 80 mm rectangular crossbars). A pitot tube was used to measure the incoming wind flow speed in different calculation lanes; the wind reduction factor was calculated using the wind speed measured at 2 m in front of the bridge model as the reference wind speed.
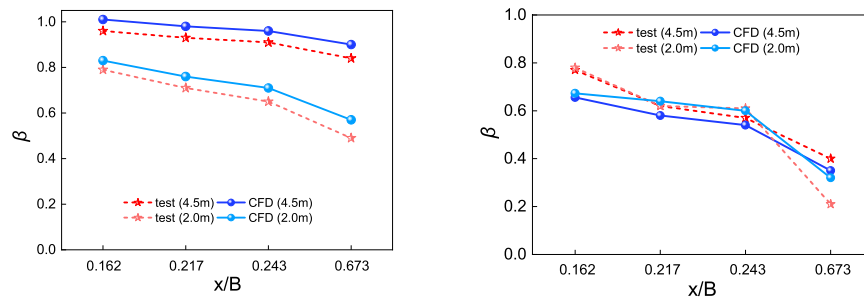
(a) variation of wind speed without wind barriers   (b) variation of wind speed with wind barriers

Fig. 8 Comparison of wind tunnel test and numerical simulation

3.2 Crosswind reduction factor

Bridge girders and additional components such as wind barriers affect the flow field in the area around them in strong winds; wind speeds vary with height above the bridge deck. To measure the wind speed, the equivalent wind speed (V_{eff}) in the vertical altitude direction above the bridge deck is defined as (Xia et al., 2017):

$$V_{eff} = \sqrt{\frac{1}{Z_r} \int_0^{Z_r} V^2(z)dz} \tag{2}$$

where Z_r is the equivalent height range influenced by lateral wind while a vehicle is driving on the bridge deck; the truck and car heights are considered to be 4.5 m and 2.0 m, respectively; V is the wind speed above the bridge deck, and z is the height above the bridge deck.

To reflect the interference effects of wind barriers, the crosswind reduction factor (CRF) β is defined as the ratio of the equivalent wind speed to the reference wind speed (incoming wind speed):

$$\beta = \frac{V_{eff}}{V_R} \tag{3}$$

where V_R is the reference wind speed for vehicle driving safety.

Figure 8 shows the wind speed variation trend at vertical heights of 2.0 m and 4.5 m above the bridge deck. The same trend is observed in the wind tunnel test and bridge deck numerical simulations with or without barriers; the wind speed gradually decreases from the flow direction to the downstream region. The extent of change gradually becomes small; there is little deviation between the results of the two methods. The wind speed above the bridge deck was reduced significantly with barriers. The numerical simulation results were in good agreement with the wind tunnel test results. A dramatic change in wind speed above the deck surface was observed in the wind tunnel test with a wind barrier installed, similar to the effects of additional fences on the turbulence characteristics of wind flow in the CFD method. The same wind-speed variation trend was observed in both methods. However, there was a slight deviation between the CFD and wind tunnel test results, within an acceptable range, possibly because the CFD-scale model used in the simulation was inconsistent with the segment model in the

wind tunnel test. The wind tunnel test and numerical simulation deviated slightly from the actual wind field. It can be concluded that greater accuracy and more reliable results can be obtained using the CFD method. Examining the static wind parameter, the $k-\varepsilon$ turbulence model was found to produce accurate force coefficients in this case study; the results demonstrate satisfactory agreement with the experimental data in analysis of the wind environment at vehicle driving level.

3.3 Field measurement

To verify the numerical simulation results and actual shielding effects of wind barriers, wind speeds were measured at vertical heights of 1.8 m and 4.5 m above the bridge deck with wind barriers (five 200 mm × 80 mm crossbars) using anemometers on Xihoumen Bridge when it was closed. NRG cup-type wind anemometers were used; the minimum and maximum wind speeds were 0.78 m/s and 96 m/s. The anemometer accuracy was ± 0.1 m/s. A vertical bar with an external diameter of 0.12 m was installed at the measurement locations to support the anemometers at different vertical heights. To decrease the shielding effects of the vertical bar on the inflow wind speed, the anemometers were fixed with lateral horizontal brackets; the horizontal distance from the anemometer to the vertical bar was 1.2 m. The field measurement layout is shown in Fig. 9. Measurement points P1–P4 correspond to the boundary between lanes A and B, the middle of lane B, the boundary between lanes B and C, and the middle of lane C on the bridge deck, respectively. The anemometer installation layout is shown in Fig. 10. With the shielding effect of the additional facilities, it was difficult to measure wind speed while the bridge was closed to traffic. The wind-speed sampling time interval was 2 s; the mean wind speed was calculated every 10 min and recorded. Two to four sets of wind speed and direction data were recorded in 40 min of continuous observation at each measurement point to ensure measurement data rationality. Figure 11 presents the range of 5-min mean wind speeds and directions in the middle of lane B, 4.5 m above the deck surface. The north direction was set as 0 for the initial angle in crosswind speed measurement. The wind speed fluctuated irregularly with time; the wind directions were almost perpendicular to the bridge axis, where the angle between the bridge axis and north was 45°.

The actual incoming wind speed was difficult to measure with the interference effects of the bridge on the wind field; thus, the wind speed monitor point was located 10 m from the leading edge (P1 in Fig. 4) in the CFD simulation analysis to evaluate the relationship between the incoming flow speed and the wind speed above the deck surface. Considering the leakage effect of the slotted parts, the wind speeds at 4.5 m above the
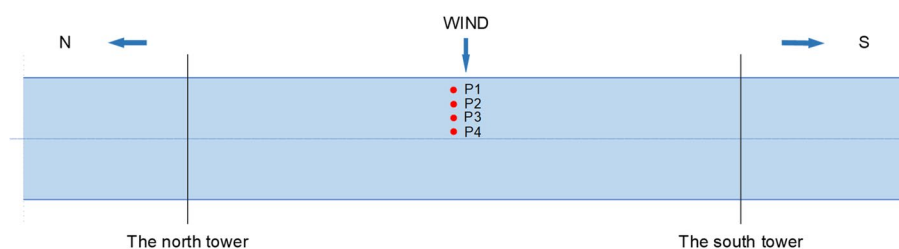

Fig. 9 Layout of field measurement

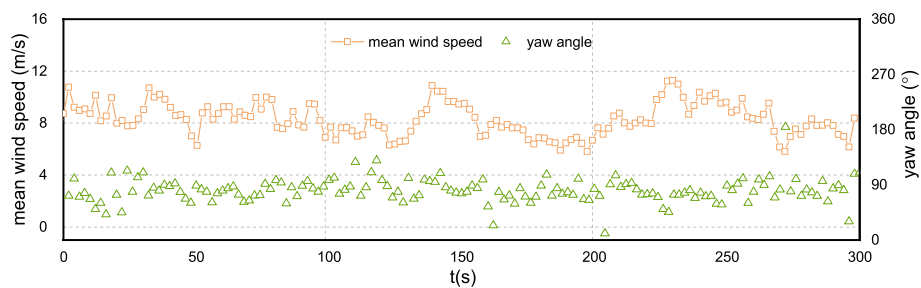**Fig. 10** Field measurement of wind environment on bridge deck

Fig. 11 Wind speeds and directions

deck in lane A, at the boundary between lanes A and B, in lane B, and at the boundary between lanes B and C were compared with the wind speed at the monitor point, as shown in Fig. 12. It is observed that the wind speed above the deck surface decreased as the distance from the leading edge increased. The proportional coefficient of the incoming wind speed and the wind speed in different lanes had a mean value of 1.59. The inflow wind speed was the actual measured wind speed at a vertical height of 6 m multiplied by the proportional coefficient. The equivalent wind speed and CRF were obtained according to the lateral wind speed distributions after the inflow wind speeds were determined.

Figure 13 compares the variations in lateral wind speed in different lanes using the three methods. In order to remove unavoidable noise during the data process, the measured wind data are filtered by a low-pass filter with a cut-off stop frequency at 5 Hz. The numerical simulation results indicate good agreement with the field measurement results; the same wind speed variation trends were observed in all lanes for the three different methods, except at the boundary between lanes A and B. The measurement results were slightly less than the experimental and simulation results at this boundary, whereas they were slightly greater than or the same at other locations. The reason for the deviation at this boundary may be that the actual wind direction was
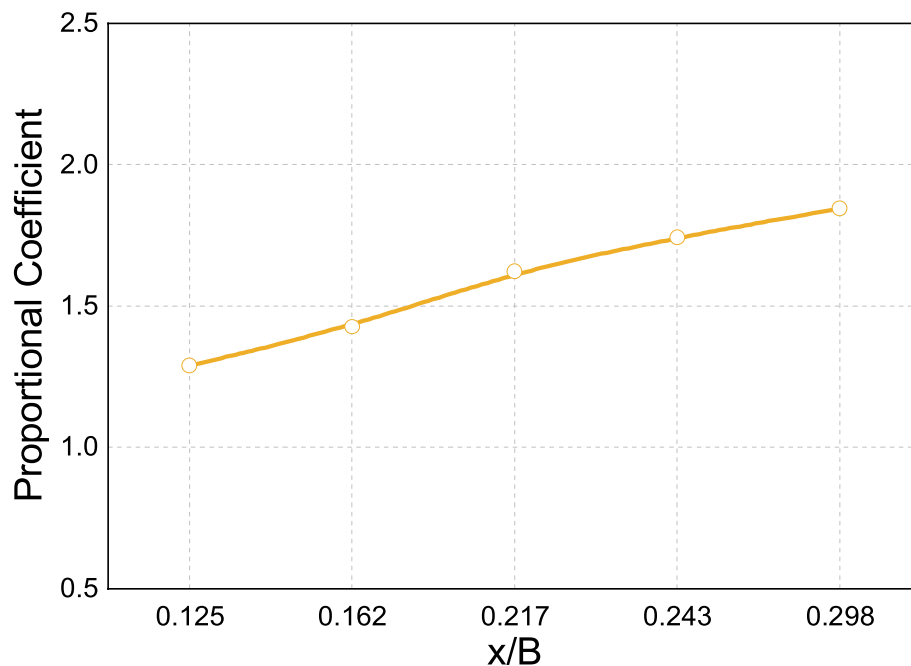
Fig. 12 Relationship between monitoring point and wind speed above deck surface (4.5 m height)

not perpendicular to the bridge axis as in the simplified ideal wind direction in the experiment and CFD. Wind speeds above the deck surface varied as the wind direction changed during field measurement.

The wind profiles in the calculation lanes are shown in Fig. 14. Compared with the results of the wind tunnel test, a smaller difference was observed between the numerical simulation and field measurement results at heights of 2 m and 4.5 m, especially at the boundary of lanes A and B at a height of 4.5 m. The deviation between the CFD and field measurement results was approximately 8.3%, within an acceptable range for engineering applications. The actual wind field and its variations were successfully reproduced using the proposed mesh generation strategy, and accurate calculation results were obtained. Wind speed increased with vertical height owing to the inertial inflow force. However, the variation was gradual from 2.0–5.0 m above the bridge deck, resulting in a decreased effect on inflow. The variation in wind speed above the wind barrier was smaller, and the effective shielded region was noticeably diminished.

4 Parameter optimization

4.1 Optimization of wind barriers

Crosswind reduction effects are sensitive to wind barrier parameters such as cross-section, height, location, porosity, and number of crossbars. Good parameter optimisation is crucial for improving reduction effects on the wind environment. Table 3 shows different wind barrier layouts; 12 types of wind barriers with different setting forms, porosities, and heights are presented in Table 4. The eighth wind barrier uses four 200 mm × 80 mm crossbars 3.6 m high; the others are 3.0 m high.
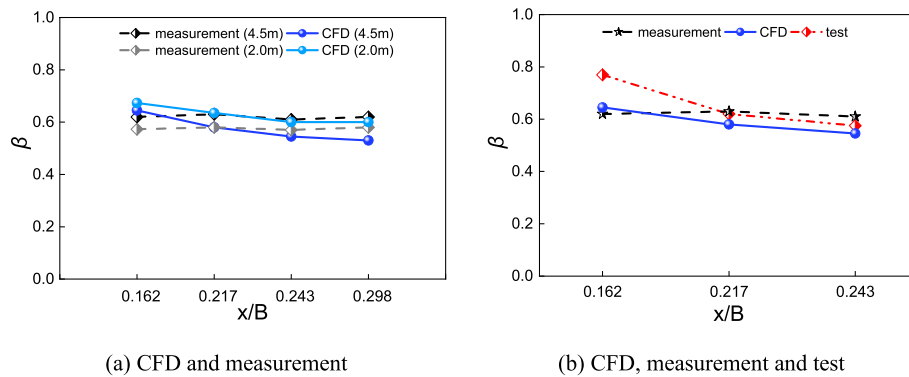
(a) CFD and measurement   (b) CFD, measurement and test

Fig. 13 Comparison of variations in lateral wind speed in different lanes by three different methods

(a) border of A and B lane   (b) B lane   (c) border of B and C lane
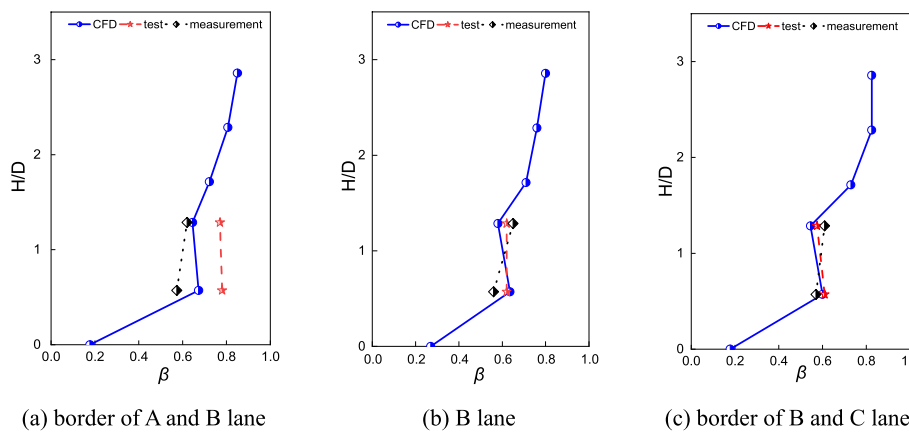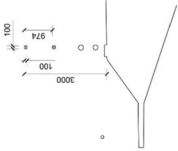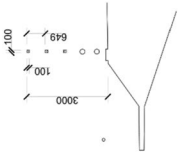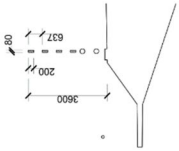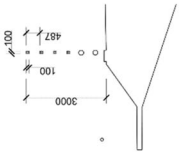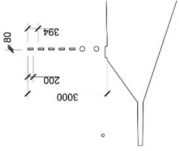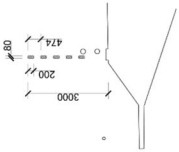
Fig. 14 Wind speed profiles over bridge deck

The wind-speed distributions in lanes with different types of wind barriers were calculated and compared. The CRFs of the lanes above the bridge deck are presented in Table 5. The wind speed decreased as the number of wind barrier crossbars increased, clearly indicating shielding effects. Optimised reduction effects were obtained with the wind barrier using five 200 mm × 80 mm crossbars. A decreasing trend was observed from the windward to leeward lanes; the CRF values were lower at the downstream deck surface than at the upstream deck surface, as shown in Table 5, indicating that wind speed was attenuated as a result of upstream and downstream wind barriers, and that the leakage effects of the slotted part of the bridge deck affected the wind speed on the downstream deck. The downstream CRF values were lower than the upstream values in all lanes. The variation became gradual due to the leakage effects of the slotted part of the bridge deck.

Figure 15 shows the wind speed variations in different lanes and the reduction effects of barriers with different crossbar sections, porosities, heights, and locations. The CRFs of wind barriers with four crossbars are compared in Fig. 15a at two heights. At the same wind barrier height, a narrower crossbar (larger aspect ratio) produces better shielding effects. The efficient shielding region increases as the crossbar cross-section increases, improving shielding effects. The crossbar cross-section is a predominant factor

Table 3 Layout of wind barrier classifications

Item	Setting scheme for wind barriers (mm)	
Number of crossbars	two 100 × 100 rectangular crossbars	three 100 × 100 rectangular crossbars
Height of crossbars	four 200 × 80 rectangular crossbars, 3.6 m	four 100 × 100 rectangular crossbars
Location of wind barriers	five 200 × 80 rectangular crossbars	five 200 × 80 rectangular crossbars, single row

Table 4 Different wind barrier types

No.	Type (mm)	Porosity	Height (m)	No.	Type (mm)	Porosity	Height (m)
1	two 100 × 100	87%	3	7	four 200 × 100	67%	3
2	two 150 × 100	84%	3	8	four 200 × 100, 3.6 m	73%	3.6
3	two 200 × 100	81%	3	9	four 200 × 80	67%	3
4	three 100 × 100	84%	3	10	four 200 × 80	61%	3
5	four 100 × 100	81%	3	11	six 150 × 80	64%	3
6	four 150 × 100	74%	3	12	five 200 × 80, single row	61%	3

influencing reduction effects. Porosity was defined as the ratio of wind barrier holes/gaps to the total area. The variation in wind speed in different lanes at the same location and height with different porosities (84%, 74%, and 64%) is shown in Fig. 15b. The reduction effect became more significant as the porosity decreased; when the porosity was reduced by 10%, the reduction effect increased by 16% according to the beta values for wind barriers with different porosities. Excessive porosity significantly reduced the effective shielding area and decreased the shielding effects; wind speed behind the wind barrier and porosity exhibited an inverse relationship. However, a porosity that is too low may cause other wind-related bridge instability issues. Considering both improvement of the wind environment and bridge aerodynamic performance, a porosity of 61% was appropriate for improving the local environment around the deck surface.

Figure 15c shows the variation in wind speed with different wind barrier heights with similar porosities (73% and 74%), indicating that crosswind reduction effects increased as the wind barrier height increased. With the same number of crossbars and the same cross-section, the porosity is also directly associated with the height of the wind barrier; the shielding effect of wind barriers on incoming flow was significantly affected by different porosities.

Figure 15d shows the influence of wind barrier location on the wind environment for the same wind barrier type and height. The reduction effects were better than with a single row when the wind barrier was in line with the balustrade. There was an overlapping part of the shielded area between the wind barriers and balustrades when the wind barrier was set as a single row; the porosity of the wind barrier as a single row was greater, resulting in a significantly reduction effect of crosswind than the wind barrier in line with the balustrades. Some conclusions can be drawn by analysing the influence of different barriers on the incoming flow. For example, the shielding effects on lateral wind speed are closely related to height, porosity, and crossbar cross-section. Porosity was the most important factor. Other factors such as height and location also reflected the influence of porosity on lateral wind speed within a certain range.

Figure 16 compares wind profiles in different lanes with and without barriers. Variations in the calculation lanes were similar in both cases. The wind speeds in lanes with wind barriers decreased by approximately 30%-50%, especially in the height range of trucks and cars, which is related to vehicle driving safety. Wind barriers had significant shielding effects; the actual efficient shielding region extended higher than the wind barrier height. The effects of wind barriers on wind speeds are more significant in leeward lanes than in windward lanes, as shown in Fig. 16. However, within a certain range, the

Table 5 CRF for different types of wind barriers

| No.	crossbars (mm)	A	B	C	upstream mean	D	E	F	downstream mean	overall mean
1	2 100 × 100	0.99	0.93	0.89	0.94	0.82	0.81	0.80	0.81	0.88
2	2 150 × 100	0.97	0.89	0.85	0.90	0.77	0.76	0.74	0.76	0.83
3	2 200 × 100	0.94	0.85	0.81	0.87	0.71	0.69	0.56	0.65	0.76
4	3 100 × 100	0.97	0.90	0.86	0.89	0.77	0.76	0.69	0.74	0.82
5	4 100 × 100	0.94	0.87	0.82	0.88	0.72	0.71	0.75	0.73	0.81
6	4 150 × 100	0.88	0.78	0.72	0.83	0.59	0.58	0.58	0.58	0.71
7	4 200 × 100	0.82	0.70	0.63	0.72	0.50	0.47	0.46	0.48	0.60
8	4 200 × 100, 3.6 m	0.83	0.71	0.67	0.74	0.54	0.52	0.50	0.52	0.63
9	4 200 × 80	0.80	0.67	0.59	0.69	0.45	0.43	0.42	0.43	0.56
10	5 200 × 80	0.71	0.58	0.51	0.61	0.35	0.33	0.32	0.33	0.47
11	6 150 × 80	0.75	0.61	0.54	0.63	0.38	0.36	0.34	0.36	0.50
12	5 200 × 80, single row	0.77	0.64	0.57	0.66	0.45	0.43	0.42	0.43	0.55

(a) cross sections   (b) porosities

(c) heights   (d) locations
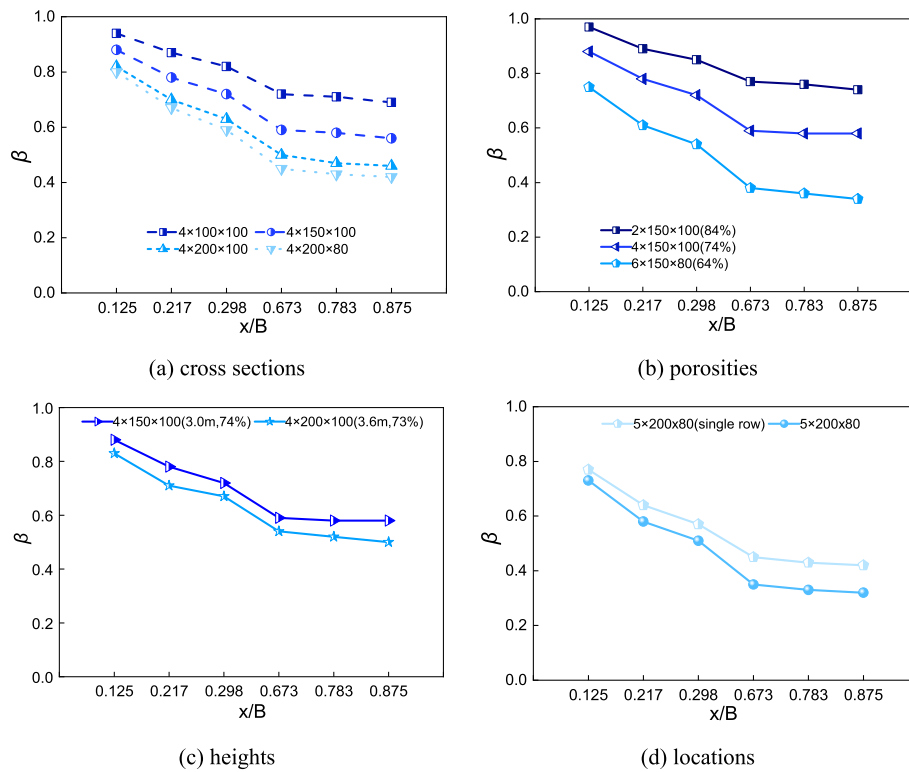
Fig. 15 Comparison of reduction effects of various type barriers
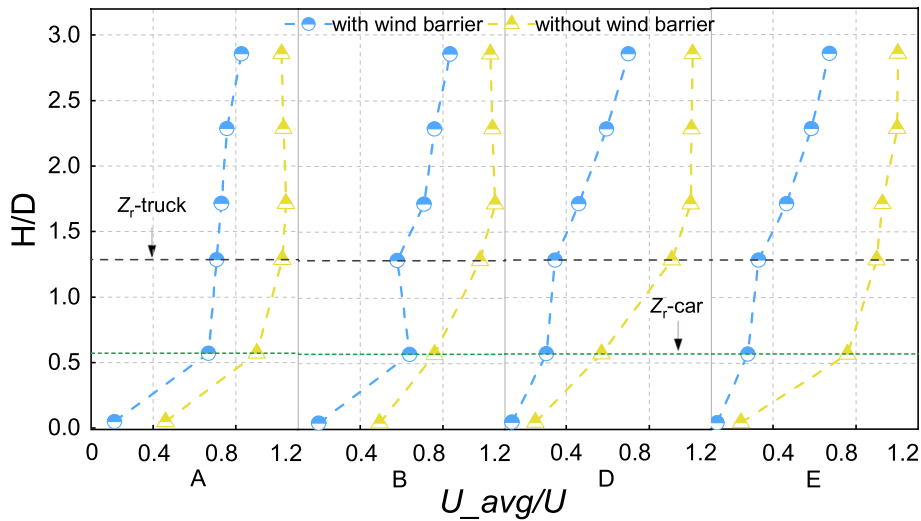

Fig. 16 Wind profiles at different lanes

shielding effect gradually weakened with distance from the top of the wind barrier. The variation in wind speed tended to be stable; no significant changes occurred at heights greater than 6 m above the deck when wind barriers were installed. The effective influence range of wind barriers was approximately twice the wind barrier height; the wind field outside that range was not affected by wind barriers.
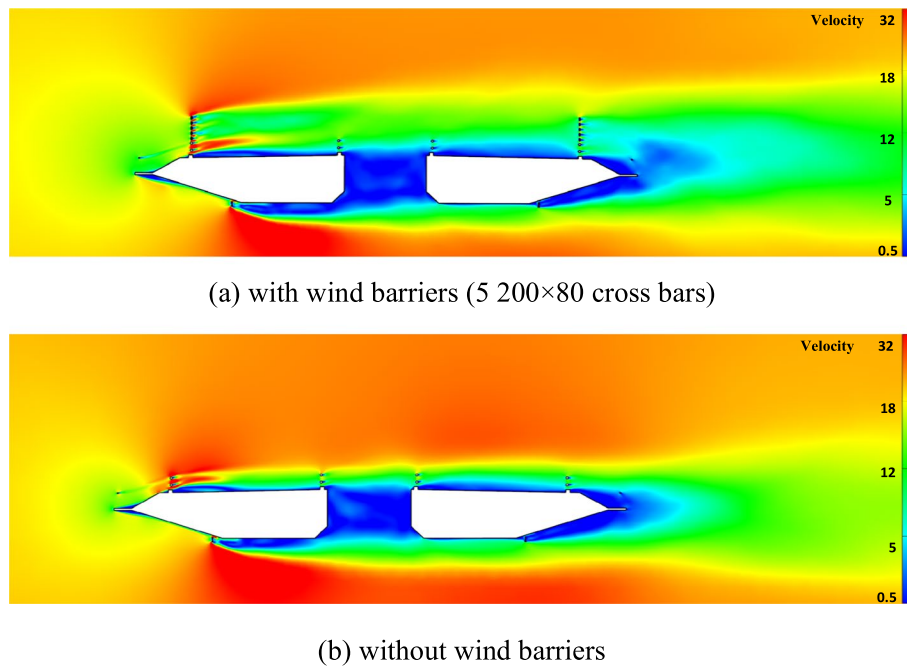
(a) with wind barriers (5 200×80 cross bars)

(b) without wind barriers

Fig. 17 Wind flow field

Figure 17 shows that with wind barriers (five 200 mm × 80 mm crossbars), wind speed was noticeably less than without wind barriers, and that wind barriers produced interference effects on incoming flow. The incoming flow was naturally separated at the edge of the windward side of the bridge. Stronger interference effects were produced by the wind barrier; vortices formed behind the wind barrier, producing stronger turbulence in the flow field around the bridge deck than with no wind barrier. A more uniform pressure was distributed on the deck surface to some extent. However, after the incoming flow was separated at the flange of the windward side, the incoming flow was separated again by the interference and separation effects of the wind barriers, and vortices were generated. Thus, a non-uniform pressure distribution field was produced around the bridge deck by the transverse vortices above the bridge deck, resulting in changes in the wind field redistribution behind the wind barriers.

As shown in Fig. 17, wind speeds were lower in the height range of the wind barriers than without wind barriers. The variation in the downstream wind speed tended to be stable; the wind speed gradually decreased as a result of wind reduction effects on the incoming flow upstream of the wind barriers. The wind field above the bridge deck beyond the range of shielding effects tended to a steady state as there was little influence from wind barriers on wind flow. According to wind speed counters, wind barriers improved the wind environment around the upstream and downstream girders compared with no wind barriers.

4.2 Impact of slotted part of bridge on wind environment

To determine the impact of the twin-box girder on the wind flow field around the bridge deck, the wind environment and speed profiles around the twin-box and overall girders were analysed. The overall box girder layout is shown in Fig. 18. The calculation lanes,
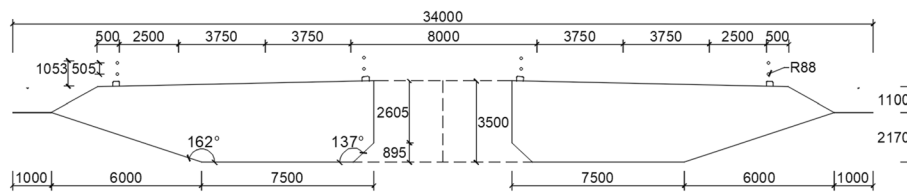
Fig. 18 Overall box girder cross section (unit: mm)

(a) regulation vortices motion through slotted part

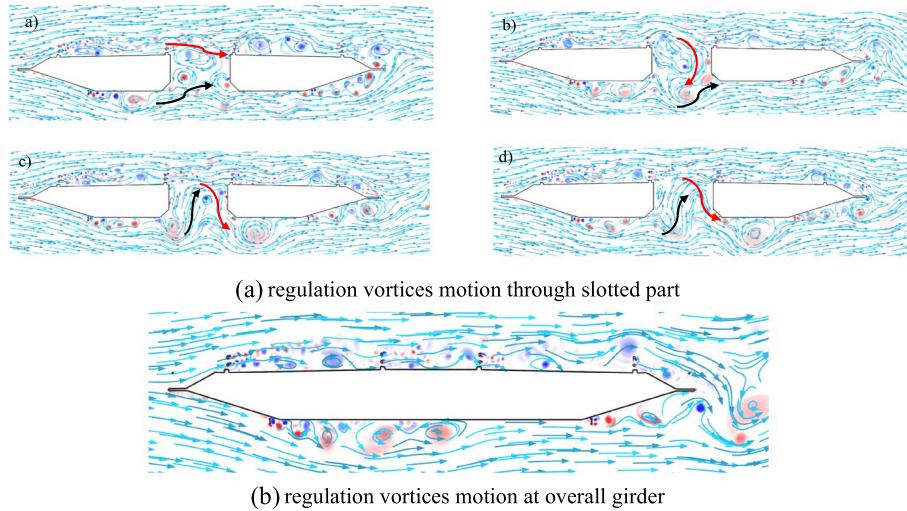(b) regulation vortices motion at overall girder

Fig. 19 Flow pattern around bridge deck

incoming flow direction, and the depth and width of the overall girder are the same as for the twin-box girder.Compared with a non-slotted girder bridge, incoming flow separation occurred at the windward side corner of the top surface of the upstream deck, and new upstream vortices formed behind the balustrades and the edge above the upstream bridge deck, as shown in Fig. 19. The wind flow separated at the maintenance rail and the windward corner of the bottom surface of the upstream deck. Thus, upstream vortices were generated under the bridge deck. Subsequently, regular vortices were formed as a result of the slotted part in the centre of the bridge. The red and black lines represent the leakage path of the flow. The upstream vortices above the bridge deck leaked downward, and the upstream vortices under the bridge deck gradually drifted upward from the slotted part. The wind speed above the downstream girder deck was less than that above the upstream girder deck because the upstream vortices leaked downward from the slotted part, causing a decrease in wind flow. However, upstream upward drifting vortices under the bridge deck were not sufficient to fill the slotted part because the upstream vortices leaking from the slots offset some of the energy of the upward drifting vortices.

The wind environment around the bridge deck and the bridge aerodynamic performance were significantly affected by the gap width in the bridge centre. Montoya et al. (2021) analysed aerodynamic interference effects between twin-box girders; the results showed that the upstream and downstream girders had significant aerodynamic interference effects on each other, especially the upstream girder on the downstream girder.

Kwok et al. ([2012](#)) and Álvarez et al. ([2018](#)) compared the effects of different gap widths on the bridge aerodynamic characteristics, reporting that as the gap width was increased, the downstream girder was gradually immersed in the wake of the upstream girder. The aerodynamic characteristics were more sensitive to different gap widths because the flow regime around the twin-box girder bridge varied with different gap widths. Li and Laima ([2015](#)) investigated the effects of the gap width on the flow characteristics around the twin-box girder; the gap ratio varied from 0.855–10.260. The experimental results showed that the flow regime around the bridge was significantly affected by the gap ratio, and the flow motion around the slotted part varied significantly with the gap width. Thus, it is evident that the effects of the gap width on the wind environment around the bridge deck are not negligible. Downstream deck wind-speed deviations between the twin-box and the overall girder were not significant. Thus, incoming flow separation occurred at the upstream corner, and a small part of the incoming flow passed through the slotted part. The influence of different gap widths on the flow regime around multi-bridge decks requires further study.

5 Conclusions

A numerical simulation was performed using a k–ε turbulence model and wall functions designed to determine the crosswind reduction effects of wind barriers on the wind environment around the Xihoumen Bridge. Wind tunnel tests and field measurements were used for verification. Wind barrier parameters were discussed for different wind barrier optimisations using the CFD method. Comparing the wind environment analyses of three methods around the bridge deck at vehicle driving level, the following conclusions can be drawn:

(1) Comparing the wind tunnel test results and CFD, the typical characteristic of the bridge model, the drag coefficient, was correctly reproduced in the simulation, indicating that the CFD method can precisely simulate the aerodynamic characteristics of the bridge deck. Field measurements also validated the calculated wind profile above the girder with satisfactory precision. Wind profiles in different calculation lanes were based on the results of experiments and field measurements; the wind environment around the bridge deck and the shielding effects of wind barriers were successfully reproduced using a flow-field discretization strategy and a CFD calculation model.

(2) The interference and shielding effects of wind barriers greatly improved the wind environment around the bridge deck. The porosity of the wind barrier was the most important factor influencing crosswind reduction effects. Lateral wind reduction of approximately 30%-50% was achieved using the optimal wind barrier, especially in the equivalent truck and car height range, where it is beneficial to vehicle driving safety. The effective wind shielding region was generally dependent on barrier height but was also related to wind barrier location and setting form. The actual effective shielding region was approximately twice the wind barrier height.

(3) Differences in the twin-box girder and the overall girder showed that the slotted part at the bridge centre had a significant influence on the wind environment around the bridge deck, especially for the downstream deck. As regular vortex motion formed as the flow passed through the slotted part, the incoming flow leaked downward, and the downstream wind speed above the leeward deck decreased significantly. Thus, the wind speeds above the leeward bridge deck were lower than those above the upstream deck

due to leakage from the slotted part of the bridge. The leakage effects on the wind environment around the twin-box girder were also affected by the gap width.

Availability of data and materials
The data and materials generated or used during the study are available from the corresponding author by request.

Declarations

Competing interests
The author(s) declared no potential conflicts of interest with respect to the research, authorship, and/or publication of this article. Advances in Bridge Engineering.

Published online: 04 July 2023

References
Álvarez AJ, Nieto F, Kwok KCS (2018) Aerodynamic performance of twin-box decks: A parametric study on gap width effects based on validated 2D URANS simulations. J Wind Eng Ind Aerod 182:202–221

Bendjebbas H, El-Hadj AA, Abbas M (2018) Numerical simulation of wind barrier openings effect on high wind speed flow around heliostats field. Appl. Math. Model 61(3):443–456

Blocken B, Stathopoulos T, Saathoff P (2008) Numerical evaluation of pollutant dispersion in the built environment: Comparisons between models and experiments. J Wind Eng Ind Aerod 96(10–11):1817–1831

Buljac A, Kozmar H, Pospiil S (2020) Effects of Wind-Barrier Layout and Wind Turbulence on Aerodynamic Stability of Cable-Supported Bridges. J Bridge Eng 25(12):04020102

Cabot, W. H. (1995), "Large-eddy simulations with wall models." Center for Turbulence Research. Annual Research Briefs: 1995 - NASA Technical Reports Server (NTRS)

Chu CR, Chang CY, Huang CJ (2013) Windbreak protection for road vehicles against crosswind. J Wind Eng Ind Aerod 116(5):61–69

Dong ZB, Luo WY, Qian GQ (2007) A wind tunnel simulation of the mean velocity fields behind upright porous fences. Agric for Meteorol 146(1–2):82–93

Frank C, Ruck B (2005) Double-arranged mound-mounted shelterbelts: Influence of porosity on wind reduction between the shelters. Eviron Fluid Mech 5(3):267–292

Gawthorpe RG (1994) Wind effects on ground transportation. J Wind Eng Ind Aerod 52(94):73–92

Hemida H, Krajnović S (2009) Exploring flow structures around a simplified ICE2 train subjected to a 30° side wind using LES. Eng Appl Comp Fluid 3(1):28–41

Hong SW, Lee IB, Seo IH (2015) Modelling and predicting wind velocity patterns for windbreak fence design. J Wind Eng Ind Aerod 142:53–64

Judd MJ, Raupach MR, Finnigan J (1996) A wind tunnel study of turbulent flow around single and multiple windbreaks, part I: Velocity fields. Bound-Lay Meteorol 80(1):127–165

Kozmar H, Procino L, Borsani A (2012) Sheltering efficiency of wind barriers on bridges. J Wind Eng Ind Aerod 107–108:274–284

Kwok KCS, Qin XR, Fok CH (2012) Wind-induced pressures around a sectional twin-deck bridge model: Effects of gap-width on the aerodynamic forces and vortex shedding mechanisms. J Wind Eng Ind Aerod 110:50–61

Li H, Laima SJ (2015) Effects of gap width on flow motions around twin-box girders and vortex-induced vibrations. J Wind Eng Ind Aerod 139:37–47

Lin M, Xin C, Wu J (2018) Aerodynamic Interference Mechanism of Moving Vehicles on a Bridge Deck in Crosswind Environment. J Bridge Eng 23(4):04018011.1–21

Ma L, Chen X, Wu J (2018) Aerodynamic interference mechanism of moving vehicles on a bridge deck in crosswind environment. J Bridge Eng 23(4):1–21

Montoya MC, Nieto F, Hernandez S (2021) Optimization of bridges with short gap streamlined twin-box decks considering structural, flutter and buffeting performance. J Wind Eng Ind Aerod 208:104316

Morden JA, Hemida H, Baker CJ (2015) Comparison of rans and detached eddy simulation results to wind-tunnel data for the surface pressures upon a class 43 high-speed train. J Fluids Eng 137(4):041108

Santiago JL, Martín F, Cuerva A (2007) Experimental and numerical study of wind flow behind windbreaks. Atmos Environ 41(30):6406–6420

Sarafrazi V, Talaee MR (2020) Comparing performances of a triangular embankment and a rigid wall-type barrier in sandstorms using simulation and a wind tunnel test. Eur Phys J E 43(12):1–15

Tominaga Y, Stathopoulos T (2009) Numerical simulation of dispersion around an isolated cubic building: Comparison of various types of k–ε models. Atmos Environ 43(20):3200–3210

Wilson JD (1985) Numerical studies of flow through a windbreak. J Wind Eng Ind Aerod 21(2):119–154

Wu FY, Wang ZL, Zhao L, et al (2023) Aerodynamic Force Distribution Characteristics around a Double-Slotted Box Girder of a Long-Span Bridge during Vortex-Induced Vibration. [J]J. Bridge Eng 28(1):04022132

Xia JL, Li K, Ge YJ (2017) Crosswind environment and flutter performances of bridge deck with different wind barriers. J Harbin Institute Technol 49(3):98–105 (In Chinese)

Yang YX, Zhang JJ, Cao FC, et al (2023) Evaluation and improvement of wind environment and vehicle safety on longspan bridge deck under strong crosswind. [J] J. Wind Eng Ind Aerodyn 228(2022):105089

Zhang T, Xia H, Guo WW (2018) Analysis on running safety of train on the bridge considering sudden change of wind load caused by wind barriers. Front Struct Civ Eng 12(4):558–567

Zhu LD, Li L, Xu YL (2012) Wind tunnel investigations of aerodynamic coefficients of road vehicles on bridge deck. J Fluid Structs 30(2):35–50

Zou YF, Qin HX, Wu T (2016) Aerodynamic performance of a novel wind barrier for train-bridge system. Wind Structs 23(3):171–189

Publisher's Note

Springer Nature remains neutral with regard to jurisdictional claims in published maps and institutional affiliations.